Inverse-Designed 90-Degree Silicon Nitride Bends for the C Band

Julian L. Pita Ruiz, Narges Dalvand, and Michaël Ménard, *Member, IEEE*

***Abstract*—We demonstrate the use of inverse design to achieve high-efficiency, compact 90° bends with radii as small as 6 μm with silicon nitride waveguides. These bends are designed for the TE polarization of single-mode waveguides with a cross-section of 850 nm × 400 nm, optimized for the C-band. Both simulations and experimental results confirm that the freeform bends obtained through inverse design outperform conventional circular and Euler bends across four footprint sizes ranging from 6 × 6 μm^2 to 21 × 21 μm^2. All inverse-designed bends were fabricated using an e-beam lithography process and designed with a minimum feature size of 160 nm, ensuring maximum compatibility with commercial optical lithography processes and viability for large-scale production. Simulations for the 6 μm radius bends show that the best freeform bend exhibits an average loss of 1.62 dB across the entire C-band, compared to 2.88 dB for circular bends and 3.46 dB for Euler bends. Experimental results align well with simulations, with measured losses of 1.89 dB, 2.86 dB, and 3.44 dB for the freeform, circular, and Euler bends, respectively. For the 11 μm bending radius, one of the freeform structures demonstrated low losses of 0.18 dB, representing reductions by factors of up to 6.6 and 1.8 times compared to Euler and circular bends, respectively. For the 16 μm and 21 μm radii, the best freeform bends achieved average losses of 0.08 dB and 0.11 dB per 90° bend across the 1530 nm to 1565 nm wavelength range. These results highlight the potential of inverse design to enable significantly more compact routing in silicon nitride photonic chips, facilitating the development of high-density photonic circuits.**

***Index Terms*—Bends, inverse design, silicon nitride, silicon photonics, topology optimization.**

I. Introduction

SILICON photonics has been widely adopted by both industry and academia as one of the most efficient platforms for integrated photonics [1], [2]. Two of the main reasons for its success are its compatibility with complementary metal-oxide-semiconductor (CMOS) fabrication processes, which enables mass production, and the high refractive index contrast between silicon and silicon dioxide, allowing for highly compact designs [3]. However, silicon nitride has emerged as a strong alternative due to material availability and a broader transparency window, extending from the visible to the mid-infrared [4]. This feature enables applications such as visible-range spectroscopy, which are beyond the capabilities of the silicon platform. Additionally, silicon nitride waveguides typically exhibit significantly lower propagation losses—often an order of magnitude lower than those of silicon in the near-infrared range [5], [6], where silicon waveguide losses generally range from 1 to 2 dB per centimeter. However, a notable drawback is the lower refractive index contrast between silicon nitride and silicon dioxide, which leads to larger device dimensions. For example, while silicon with a 220 nm thickness allows for a minimum bend radius of around 5 μm to avoid significant losses in 90° bends [7], silicon nitride with a thickness of 400 nm requires a much larger bend radius of approximately 50 μm [8]. This increased bend radius enlarges the device and routing footprint, directly impacting fabrication costs.

Several methods, primarily developed on silicon platforms, have been proposed to reduce losses in small routing bends. These include techniques such as spline curves [9], [10], corner bends [11], Euler and partial Euler bends [12], [13], [14], Bezier bends [15], [16], [17], subwavelength grating bends [18], [19], [20], advanced waveguide bends [21], [22], n-adjustable bends [23], [24], asymmetric coupler waveguides [25], inverse-designed bends [26], [27], [28], [29], and even combinations of these approaches [30]. On silicon nitride platforms, Vogelbacher et al. demonstrated 90° partial Euler bends with a bending radius of 50 μm in waveguides with a cross-section of 700 nm × 150 nm at 850 nm, achieving a low loss of 0.01 dB for the TE mode [14]. Similarly, at the same wavelength, Song et al. demonstrated advanced waveguide bends with radii as small as 5 μm, achieving losses of 1.81 dB per 90° bend. For 20 μm bends, they achieved losses as low as 0.01 dB per 90°, using waveguides with a 600 nm width and 300 nm thickness [21]. In the C-band at 1550 nm, Gao et al. demonstrated 30 μm advanced bends with a loss of 0.037 dB per 90° in waveguides measuring 1 μm in width and 400 nm in thickness [22]. Additionally, Sun et al. demonstrated compact silicon nitride Bezier bends with radii as small as 8 μm, achieving a loss of 0.95 dB per 90° bend using waveguides with a cross-section of 1220 nm × 400 nm [17]. It is important to note that both demonstrations at 1550 nm used waveguides capable of supporting higher-order modes.

Despite significant advancements in reducing bending losses on silicon nitride platforms, small bends remain little explored.

Received 4 January 2025; revised 5 March 2025; accepted 19 March 2025. Date of publication 24 March 2025; date of current version 16 June 2025. This work was supported in part by PRIMA Quebec under Grant R16-46-002 PSO, in part by AEPONYX Inc., in part by the Natural Sciences and Engineering Research Council of Canada under Grant CRDPJ 530551 - 18, and in part by CMC Microsystems through the fabrication of the devices at Applied Nanotools (ANT). *(Corresponding author: Narges Dalvand.)*

The authors are with the Department of Electrical Engineering, École de Technologie Supérieure, Montreal, QC H3C 1K3, Canada (e-mail: julian-leonel.pita-ruiz@etsmtl.ca; narges.dalvand.1@ens.etsmtl.ca; michael.menard@etsmtl.ca).

Color versions of one or more figures in this article are available at https://doi.org/10.1109/JLT.2025.3554096.

Digital Object Identifier 10.1109/JLT.2025.3554096

Even the inverse design technique, which has been successfully applied to compact silicon devices in recent years [31], has rarely been used with silicon nitride, with only a few exceptions such as polarizers [32], switches [33], and reflectors [34]. In this article, we demonstrate eight topology-optimized bends in silicon nitride with footprints ranging from $6 \times 6\,\mu\mathrm{m}^2$ to $21 \times 21\,\mu\mathrm{m}^2$ for use in the C-band. For each bend radius, we fabricated two inverse-designed prototypes (ID1 and ID2): ID1, where the entire design region is filled with silicon dioxide or silicon nitride as the initial condition, and ID2, where a circular bend is used as the initial condition. Our results show that the freeform structures outperform both Euler and circular bends with a comparable footprint. Simulations predict average losses across the entire C-band of around $0.04\,\mathrm{dB}$ per 90° bend for the $16\,\mu\mathrm{m}$ and $21\,\mu\mathrm{m}$ freeform bends, and up to $0.17\,\mathrm{dB}$ per 90° for the $11\,\mu\mathrm{m}$ bend. For the inverse-designed bend with a $6\,\mu\mathrm{m}$ radius, we observe up to a $2.14\times$ reduction in losses compared to circular and Euler bends. Notably, experimental results show good agreement with simulations, with average measured losses in the C-band of $1.86\,\mathrm{dB}$, $0.18\,\mathrm{dB}$, $0.08\,\mathrm{dB}$, and $0.11\,\mathrm{dB}$ for optimization regions of $6 \times 6\,\mu\mathrm{m}^2$, $11 \times 11\,\mu\mathrm{m}^2$, $16 \times 16\,\mu\mathrm{m}^2$, and $21 \times 21\,\mu\mathrm{m}^2$, respectively.

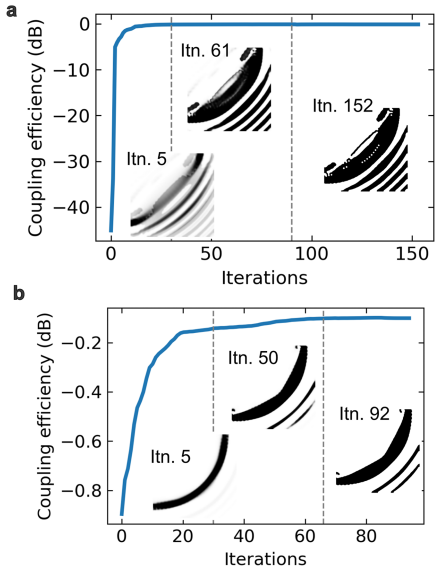

Fig. 1. Optimization trajectory for inverse-designed $11\,\mu\mathrm{m} \times 11\,\mu\mathrm{m}$ bends. (a) optimization process with silicon dioxide filling the entire design space as the initial condition and (b) optimization process using a circular bend as the initial condition. Each figure is accompanied by three insets depicting the refractive index distribution at each stage of the optimization process.

II. Design and Simulation

The devices were designed on a platform consisting of a $400\,\mathrm{nm}$ thick silicon nitride layer with silicon dioxide bottom and top claddings of $4.5\,\mu\mathrm{m}$ and $3\,\mu\mathrm{m}$, respectively. The 90° bends were optimized using topology optimization via the Lumopt, a Python-based continuous adjoint optimization wrapper that employs 3D FDTD to solve the direct and adjoint problems. Four square optimization regions, ranging from $6 \times 6\,\mu\mathrm{m}^2$ to $21 \times 21\,\mu\mathrm{m}^2$ in size, with increments of $5\,\mu\mathrm{m}$, were employed to compare the performance of the resulting freeform structures against conventional bends with the same radius as the side length of the optimization regions. The devices were designed for the TE mode, with input and output waveguides featuring cross-sections of $850\,\mathrm{nm} \times 400\,\mathrm{nm}$. The optimization process targeted the C-band, aiming to maximize coupling efficiency at the output waveguide over five wavelengths between $1530\,\mathrm{nm}$ and $1565\,\mathrm{nm}$. To enhance compatibility with commercial CMOS foundries, the minimum feature size was constrained to $160\,\mathrm{nm}$, and a smoothing filter with a radius of $160\,\mathrm{nm}$ was applied during the optimization process to eliminate small islands and sharp corners. As initial conditions for the optimization, we explored two different scenarios: one with the entire design space filled with silicon nitride or silicon dioxide (ID1), and the other with circular bends (ID2). Notably, positioning the input and output waveguides at the corners of each optimization region did not yield optimal performance. Instead, consistently better results were obtained by placing the waveguides about $1.4\,\mu\mathrm{m}$ away from the corner of the optimization regions. Nevertheless, the dimensions of the optimization regions were kept the same. As a results, you can see features below the input waveguides in Fig. 2 for the inverse designs, but note that there are none on the top part. Hence, the area occupied by the bends is shifted to the bottom right with respect to the conventional designs.

Fig. 1 presents the optimization trajectory of the inverse-designed bend, comparable to a $11\,\mu\mathrm{m}$ radius bend, with the entire design region filled with silicon dioxide as the initial condition (Fig. 1(a)) and with a circular bend as the initial condition (Fig. 1(b)). The trajectory encompasses the three stages of the optimization process: the greyscale stage (set to 30 iterations), followed by the binarization and design-for-manufacturing (DFM) stages. Notably, throughout all three stages, there was no significant drop in coupling efficiency, indicating an effective binarization and a successful imposition of the fabrication constraints. Both optimization trajectories converge to a similar coupling efficiency value of approximately $-0.17\,\mathrm{dB}$. However, the optimization starting with the circular bend begins at around $-0.9\,\mathrm{dB}$, whereas the optimization starting with silicon dioxide begins below $-40\,\mathrm{dB}$. Importantly, in both cases, the objective converges rapidly during the greyscale stage and maintains this value throughout the subsequent stages, underscoring the efficiency of the optimization process. Additionally, Fig. 1(a) and (b) include three insets showing the refractive index distribution at the different stages of the optimization process. In both cases, it is apparent that the final geometry features a wider, non-uniform bent waveguide, possibly indicating that the structure is attempting to reduce losses caused by mode mismatch. Moreover, a non-uniform 1D photonic crystal-like structure adjacent to the bent waveguide is also observed, which seems to be aimed at mitigating radiation losses due to the bend. Although the solutions can be considered local optima, they demonstrate consistency, as we obtained similar results multiple times and achieved nearly symmetric structures without explicitly enforcing symmetry.

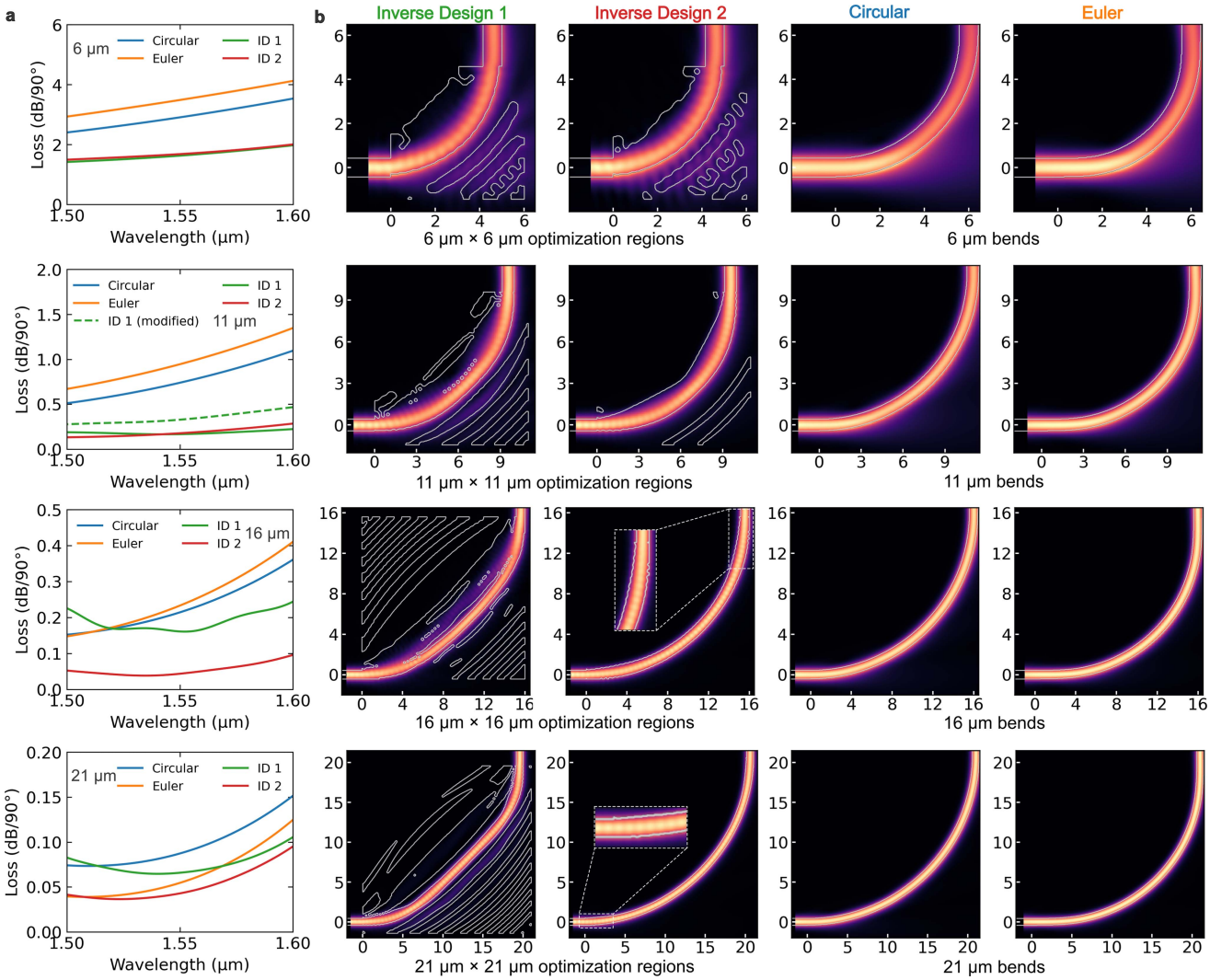

Fig. 2. Simulation results for all inverse-designed bends compared with circular and Euler bends of comparable footprints. (a) Coupling efficiency of the bends across a wavelength range from 1500 nm to 1600 nm for each footprint size. (b) Magnitude of the electric field at 1550 nm, superimposed over a contour of the geometry for all bends for each footprint size. The ID2 figures for the 16 μm and 21 μm bends include insets zooming in on intricate features at the input and output waveguide interfaces, respectively.

Fig. 2(a) shows the losses of the ID1 and ID2 bends, along with a circular and Euler bend, across a wavelength range from 1500 nm to 1600 nm for all four footprint sizes. There are two main takeaways from the simulation results. First, the average losses across the simulated wavelength range are lower for all inverse-designed bends compared to the corresponding circular and Euler bends. Secondly, the variation in losses over the wavelength range is also smaller for the inverse-designed bends. For instance, in the smallest simulated bends, we observe a variation in losses of 1.1 dB for the circular bend, whereas the ID2 bend exhibits only a 0.5 dB variation. Additionally, in the $16 \times 16\ \mu\text{m}^2$ freeform bends, ID1 performs significantly worse than ID2. This difference in performance is attributed to the positioning of the input and output waveguides during the optimization setup—ID1 has the waveguides placed at the corner of the optimization region, whereas ID2 has the waveguides offset by about 1.4 μm from the corner, resulting in better performance. Furthermore, as the bend size increases, losses decrease, with the ID2 bend for the $21 \times 21\ \mu\text{m}^2$ footprint achieving the lowest loss of just 0.042 dB, outperforming all other bends. In addition, although the bends were optimized for the TE polarization, the design also helps reduce the bend losses of the TM mode. For instance, for the 6 μm bends, the losses are 6.2 dB, 7.01 dB, 3.39 dB, and 3.96 dB for the circular, Euler, ID1, and ID2 bends, respectively.

Fig. 2(b) illustrates the magnitude of the electric field at 1550 nm, superimposed over the contour geometry of each bend design. Optical losses in waveguide bends generally arise from material absorption, scattering due to undesired surface roughness, radiation losses caused by waveguide curvature, and mode mismatch [35]. In these simulations, material absorption and roughness-induced scattering were excluded, as they depend heavily on fabrication conditions, for which we lack data to model accurately. Therefore, our focus is on losses due to curvature and mode mismatch. For smaller bend radii, mode mismatch and radiation losses dominate. This is evident in the

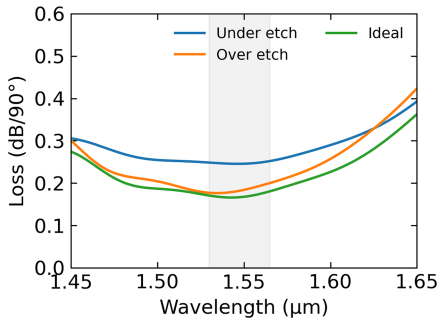

Fig. 3. Simulation results for the $11 \times 11\,\mu\mathrm{m}^2$ optimized bend, including the effects of fabrication variations. The shaded grey region highlights the C-band.

electric field profiles of Fig. 2(b), especially for the smallest bends, where more significant field leakage indicates higher losses.

The ID1 designs feature bent waveguides with non-uniform widths and intricate geometries, including the presence of holes, particularly in the $11 \times 11\,\mu\mathrm{m}^2$ and $16 \times 16\,\mu\mathrm{m}^2$ configurations. Additionally, a non-uniform 1D photonic crystal-like structure emerges adjacent to the bent waveguide, likely playing a critical role in minimizing curvature-related radiation losses. For instance, for $11\,\mu\mathrm{m}$ radius bends, removing this 1D photonic crystal-like structure in the ID1 design increases the losses by 1.9 times, as shown by the green dotted line in Fig. 2(a). It is also important to note that this structure helps equalize the losses across the entire range. On the other hand, in the ID2 structures, this non-uniform 1D photonic crystal-like structure is absent in larger designs (e.g., the $21\,\mu\mathrm{m} \times 21\,\mu\mathrm{m}$ footprint). However, some intricate roughness is observed at the interfaces between the bent waveguides and the straight input/output waveguides, as highlighted in the insets. This roughness likely helps reduce losses by improving mode matching at the waveguide transitions. It is also worth noting that for the $6\,\mu\mathrm{m}$ and $11\,\mu\mathrm{m}$ radius bends, the circular bends demonstrate better performance than the Euler bends across the entire simulated wavelength range.

To assess the robustness of the devices against fabrication variations, we simulated two scenarios for the $11 \times 11\,\mu\mathrm{m}^2$ optimized bend: one with lateral over-etching of approximately $30\,\mathrm{nm}$ and vertical over-etching of $10\,\mathrm{nm}$, and another with under-etching of approximately $30\,\mathrm{nm}$. Fig. 3 presents the losses for these variations compared to the ideal design across the S, C, and L bands. The results indicate that simulated over-etching has minimal impact on losses in the C band but significantly affects the L band. In contrast, simulated under-etching increases the average losses across the entire C band by a factor of $1.46\times$, while having a smaller impact on the regions most affected by over-etching. These findings highlight the robustness of the design to over-etching variations, a characteristic that is further validated by experimental results.

III. Results

The devices were fabricated in a Multi-Project Wafer run at ANT where the silicon nitride is fully etched. The process utilized silicon wafers with thickness of $525\,\mu\mathrm{m}$, along with a bottom thermal oxide layer of $4.5\,\mu\mathrm{m}$ and a top cladding oxide layer of $3\,\mu\mathrm{m}$, deposited using plasma-enhanced chemical vapor deposition (PECVD). Patterning was performed using 100 keV electron beam lithography, employing a proximity effect correction algorithm to mitigate electron scattering effects. This was done on a silicon nitride layer with a thickness of $400\,\mathrm{nm}$. The structures were subsequently etched using an anisotropic ICP-RIE process, resulting in features with sidewall angles of approximately $83.5°$. The fabrication process supported a minimum feature size of $120\,\mathrm{nm}$ and a minimum feature spacing of $120\,\mathrm{nm}$, yielding TE optical losses of around $1\,\mathrm{dB/cm}$ for waveguides with a width of $850\,\mathrm{nm}$ at a wavelength of $1550\,\mathrm{nm}$. Fig. 4 presents scanning electron microscopy (SEM) images of the fabricated inverse-designed bends for all four footprints. The majority of the design features are visible in these images, including the intricate roughness and non-uniform 1D photonic crystal-like structures seen in all ID1 designs. Specifically, for the ID1 bends with $11 \times 11\,\mu\mathrm{m}^2$ and $16 \times 16\,\mu\mathrm{m}^2$ footprints, all the small holes appearing during the optimization are clearly present. Additionally, the insets highlight the intricate roughness at the interfaces between the bends and the straight waveguides, as shown in the inset of Fig. 4. The fabricated devices exhibit good agreement with the designed structures, suggesting that their performance should be close to what was predicted in simulations.

To measure the efficiency of each $90°$ inverse-designed bend, as well as the circular and Euler bends, we fabricated sets of $90°$ bends connected in series for each bend design, spanning all footprints. For the $6\,\mu\mathrm{m}$ bend radii, we fabricated configurations with 2, 4, and 8 bends; for the $11\,\mu\mathrm{m}$ bend radii, we used 8, 12, and 16 bends; for the $16\,\mu\mathrm{m}$ bend radii, we included 12, 16, and 20 bends; and finally, for the $21\,\mu\mathrm{m}$ bend radii, we arranged 20, 28, and 36 bends in series. Each series of bends was connected to a grating coupler at both the input and output ends. The grating coupler used for the experiments was designed using the Spins-B software [36], with a minimum feature size of $400\,\mathrm{nm}$. Under ideal conditions (i.e., with no gap between the fiber and the chip), it exhibits a simulated coupling efficiency of $3.25\,\mathrm{dB}$ and has a 3-dB bandwidth of $178\,\mathrm{nm}$. For the measurements, we employed a straightforward optical setup consisting of a TC100S-HP laser from EXFO, a TE-polarization-maintaining $30°$ fiber array, and an EXFO CT440 tester. We maintained consistent experimental conditions across all measurements, particularly with respect to the coupling distance which was set to $50\,\mu\mathrm{m}$. Additionally, we positioned the sets of bends with the same footprint as close as possible to one another on the chip to minimize potential fabrication variations due to the device placement on the die.

Fig. 5(a) and (c) present the experimental results for the inverse-designed bends in comparison with circular and Euler bends across the four evaluated footprints. In Fig. 5(a), the scatter plot shows the average transmission for each test structure, which consists of a series of bends connected with corresponding input and output grating couplers. Each data set is accompanied by a fitted linear equation derived from the average transmission across the entire C-band, facilitating the extraction of two key

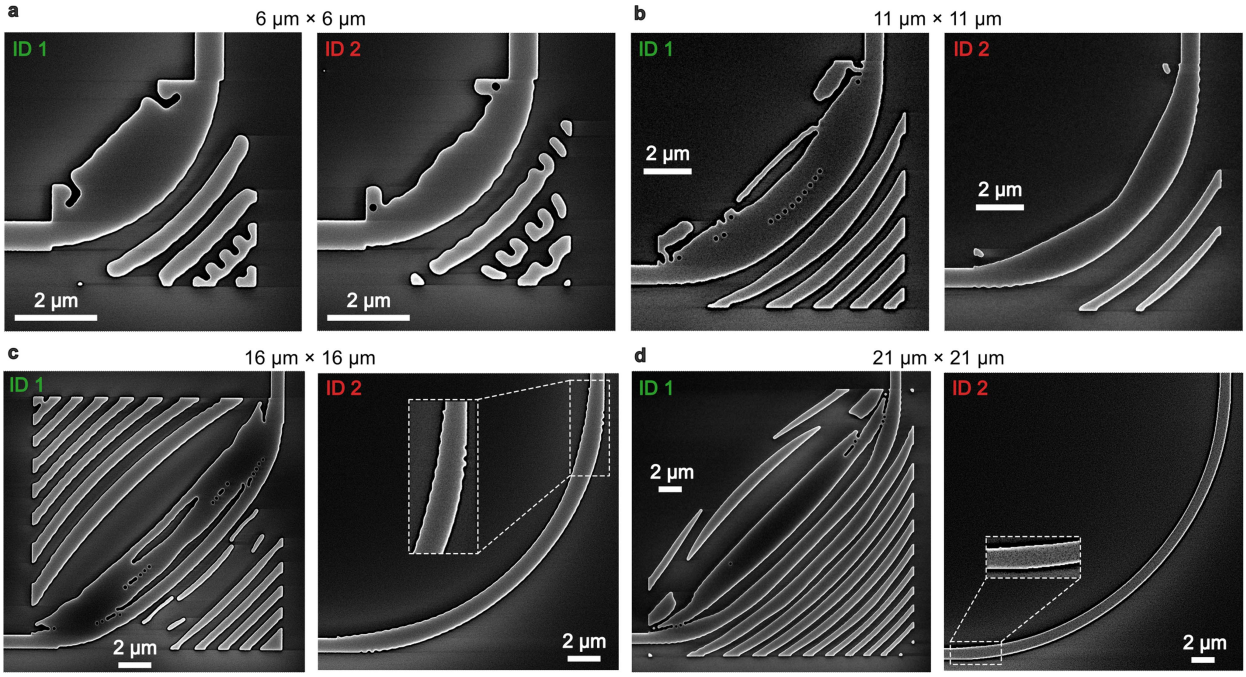

Fig. 4. SEM images of the fabricated silicon nitride inverse-designed bends. The images show bends with varying footprints: (a) $6\,\mu\text{m} \times 6\,\mu\text{m}$, (b) $11\,\mu\text{m} \times 11\,\mu\text{m}$, (c) $16\,\mu\text{m} \times 16\,\mu\text{m}$, and (d) $21\,\mu\text{m} \times 21\,\mu\text{m}$. The labels ID1 and ID2 indicate two inverse-designed bends obtained using different initial conditions: ID1 uses silicon oxide as the starting geometry, whereas ID2 starts from a circular bend. Insets in (c) and (d) highlight the intricate roughness present at the interfaces between the bend and the input/output waveguides, which may contribute to improved mode matching.

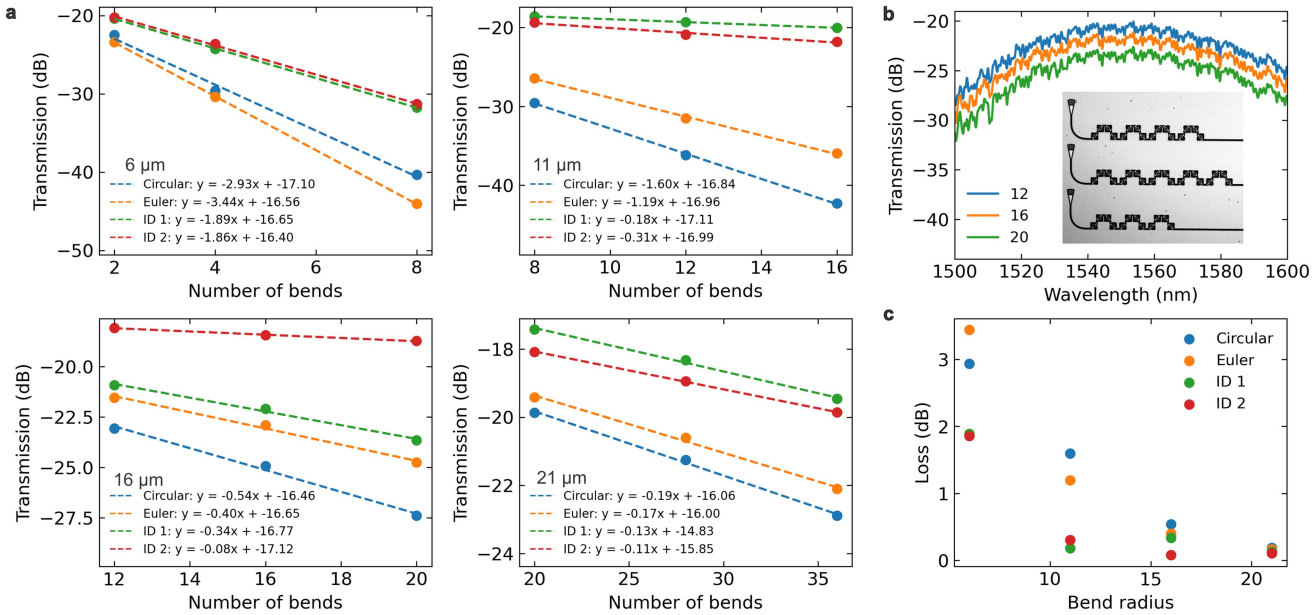

Fig. 5. Measurement results for the fabricated silicon nitride bends. (a) Measured average losses in the C-band and their corresponding linear fits, with the resulting fitted equations included in the legend for each bend type, evaluated for radii of $6\,\mu\text{m}$, $11\,\mu\text{m}$, $16\,\mu\text{m}$, and $21\,\mu\text{m}$. The slope of each fit line represents the loss per 90° bend, whereas the y-intercept relates to the grating losses. (b) Raw measurements for the ID2 bend with a $16\,\mu\text{m} \times 16\,\mu\text{m}$ footprint over a wavelength range of 1500 nm to 1600 nm, alongside an inset showing an image of the tested devices. (c) Extracted losses for the inverse-designed bends (ID1 and ID2) compared to traditional circular and Euler bends across different footprint sizes.

parameters: the insertion loss per 90° bend and the grating loss. From the linear fit, the slope of each line represents the loss per individual bend structure, whereas the y-intercept indicates the combined loss of the input and output grating couplers. Notably, the inverse-designed bends, labeled as ID1 and ID2, consistently demonstrate lower losses compared to the circular and Euler bends with a comparable footprint. For example, for the $6\,\mu\mathrm{m}$ radius bends, the measured losses are $2.93\,\mathrm{dB}$ for the Euler bend and $3.44\,\mathrm{dB}$ for the circular bend. In contrast, the losses for the inverse-designed ID1 and ID2 bends are significantly lower, at $1.89\,\mathrm{dB}$ and $1.86\,\mathrm{dB}$, respectively. This represents a reduction in loss by up to 1.8 times when comparing the inverse-designed bends with the conventional bends.

Interestingly, the lowest measured losses of $0.08\,\mathrm{dB}$ were observed for the structure with a footprint of $16 \times 16\,\mu\mathrm{m}^2$, rather than the $21 \times 21\,\mu\mathrm{m}^2$ footprint, which exhibited losses around $0.11\,\mathrm{dB}$. This finding contradicts the simulation results, which predicted losses of $0.043\,\mathrm{dB}$ and $0.042\,\mathrm{dB}$ for both footprints, respectively. The discrepancy between the simulated and measured results could be attributed to fabrication defects, potentially impacting the performance of the larger footprint designs. The losses obtained per grating range between $7.45\,\mathrm{dB}$ and $8.56\,\mathrm{dB}$, which is considerably higher than the values predicted by simulations under ideal conditions. However, it is crucial to note that these measurements were taken with a $50\,\mu\mathrm{m}$ gap between the fiber and the chip, which adds approximately $2.6\,\mathrm{dB}$ of loss per grating. After adjusting for this gap-induced loss, the estimated grating losses fall between $4.5\,\mathrm{dB}$ and $5.96\,\mathrm{dB}$, aligning more closely with the simulated results. The remaining discrepancies could be attributed to fabrication variations, and the differences in grating losses across devices may also be influenced by the specific position of the devices on the die. Fig. 5(b) displays the raw measurements for the ID1 design with a $16\,\mu\mathrm{m} \times 16\,\mu\mathrm{m}$ footprint over a wavelength range from $1500\,\mathrm{nm}$ to $1600\,\mathrm{nm}$, taken for configurations with 12, 16, and 20 bends. This data yielded a fitted loss of $0.34\,\mathrm{dB}$ per 90° bend, with a combined loss of $16.77\,\mathrm{dB}$ attributed to the two grating couplers. Fig. 5(c) summarizes the extracted per-bend losses obtained from the linear fitting process across all evaluated footprint sizes. It is evident that the inverse-designed bends (ID1 and ID2) exhibit lower losses compared to the circular and Euler bends, especially for footprint sizes up to $16\,\mu\mathrm{m}$ bend radii. Although the performance advantage of the inverse-designed bends diminishes for larger bend radii, such as $21\,\mu\mathrm{m}$, ID2 still achieves a loss of $0.11\,\mathrm{dB}$, which is lower than the $0.19\,\mathrm{dB}$ loss observed for the Euler bend, demonstrating the continued efficacy of inverse design even at larger bend sizes.

IV. Discussion and Conclusion

In this work, we introduced eight freeform, compact inverse-designed bends implemented on a silicon nitride platform. Both simulation and experimental results confirm that the inverse-designed structures outperform conventional circular and Euler bends with comparable footprints. Although inverse design has been widely explored in silicon photonics, leading to compact devices with efficiencies comparable to larger structures developed through traditional methods, it has seen less application in medium index contrast platforms such as silicon nitride, where it nevertheless has significant potential.

Traditional photonic design approaches rely heavily on deep physical insight, intuition, and iterative simulations to optimize device performance. Although inverse design also requires a profound understanding of physics, it facilitates the exploration of unconventional geometries that extend beyond traditional intuition, yielding enhanced performance. Successful inverse design relies on a careful selection of the initial conditions, optimization region size, and appropriate fabrication constraints to ensure robustness. In some cases, the problem must be decomposed into smaller parts to achieve optimal results. For instance, the inverse-designed bends with a $16 \times 16\,\mu\mathrm{m}^2$ footprint, designed with a minimum feature size of $160\,\mathrm{nm}$ (readily achievable in commercial foundries), resulted in structures featuring wide, non-uniform bent waveguides. At the interface between the bend and the straight waveguide, we observed an offset similar to techniques used previously to improve compact bend efficiency. Additionally, the design yielded a non-uniform 1D photonic crystal structure adjacent to the bent waveguide, effectively reducing bend losses. This structural approach could potentially inspire improvements in conventional circular and Euler bend designs.

The inverse-designed bends demonstrated high performance in silicon nitride, achieving losses as low as $0.08\,\mathrm{dB}$ per 90° bend for TE polarization, with bend radii comparable to $16\,\mu\mathrm{m}$. These results surpass those of traditional bend designs and exhibit a high degree of robustness to fabrication variations, particularly to over-etching scenarios. Overall, inverse design proves to be a powerful tool for creating non-intuitive, high-efficiency photonic structures, pushing the boundaries of what is achievable with conventional methods. This work highlights the potential of inverse design to unlock new possibilities in photonic device engineering, particularly for platforms with moderate index contrast such as silicon nitride.

Acknowledgment

The authors express their gratitude to Calcul Québec for providing access to computing servers for the optimization process.

References

[1] S. Y. Siew et al., "Review of silicon photonics technology and platform development," *J. Lightw. Technol.*, vol. 39, no. 13, pp. 4374–4389, Jul. 2021.
[2] C. Xiang, S. M. Bowers, A. Bjorlin, R. Blum, and J. E. Bowers, "Perspective on the future of silicon photonics and electronics," *Appl. Phys. Lett.*, vol. 118, no. 22, 2021, Art. no. 220501.
[3] M. A. Tran et al., "Extending the spectrum of fully integrated photonics to submicrometre wavelengths," *Nature*, vol. 610, no. 7930, pp. 54–60, 2022.
[4] R. Baets et al., "Silicon photonics: Silicon nitride versus silicon-on-insulator," presented at Opt. Fiber Commun. Conf., Anaheim, CA, USA, Mar. 20–22, 2016, Paper Th3J.1.
[5] Z. Ye et al., "Foundry manufacturing of tight-confinement, dispersion-engineered, ultralow-loss silicon nitride photonic integrated circuits," *Photon. Res.*, vol. 11, no. 4, pp. 558–568, 2023.
[6] K. A. Buzaverov et al., "Silicon nitride integrated photonics from visible to mid-infrared spectra," *Laser Photon. Rev.*, vol. 18, 2024, Art. no. 2400508.

[7] M. Bahadori, M. Nikdast, Q. Cheng, and K. Bergman, "Universal design of waveguide bends in silicon-on-insulator photonics platform," *J. Lightw. Technol.*, vol. 37, no. 13, pp. 3044–3054, Jul. 2019.
[8] C. Xiang, W. Jin, and J. E. Bowers, "Silicon nitride passive and active photonic integrated circuits: Trends and prospects," *Photon. Res.*, vol. 10, no. 6, pp. A82–A96, 2022.
[9] Z. Hu and Y. Y. Lu, "Computing optimal waveguide bends with constant width," *J. Lightw. Technol.*, vol. 25, no. 10, pp. 3161–3167, Oct. 2007.
[10] E. Zhang, S. Yang, and L. Zhang, "General waveguide bend design based on cubic spline interpolation and inverse design," *J. Lightw. Technol.*, vol. 42, no. 13, pp. 4614–4625, Jul. 2024.
[11] Y. Wang and D. Dai, "Multimode silicon photonic waveguide corner-bend," *Opt. Exp.*, vol. 28, no. 7, pp. 9062–9071, 2020.
[12] M. Cherchi, S. Ylinen, M. Harjanne, M. Kapulainen, T. Vehmas, and T. Aalto, "The Euler bend: Paving the way for high-density integration on micron-scale semiconductor platforms," *Proc. SPIE*, vol. 8990, pp. 20–26, 2014.
[13] M. Cherchi, S. Ylinen, M. Harjanne, M. Kapulainen, and T. Aalto, "Dramatic size reduction of waveguide bends on a micron-scale silicon photonic platform," *Opt. Exp.*, vol. 21, no. 15, pp. 17814–17823, 2013.
[14] F. Vogelbacher, S. Nevlacsil, M. Sagmeister, J. Kraft, K. Unterrainer, and R. Hainberger, "Analysis of silicon nitride partial Euler waveguide bends," *Opt. Exp.*, vol. 27, no. 22, pp. 31394–31406, 2019.
[15] D. Yi, Y. Zhang, and H. K. Tsang, "Optimal Bezier curve transition for low-loss ultra-compact S-bends," *Opt. Lett.*, vol. 46, no. 4, pp. 876–879, 2021.
[16] T. Y. Ang, J. R. Ong, S. T. Lim, C. E. Png, X. Guo, and H. Wang, "Versatile Bezier bends for silicon photonics," presented at Lasers and Electro-Optics Pacific Rim, Singapore, Jul. 2017, Paper s1869.
[17] T. Sun and M. Xia, "Low loss modified Bezier bend waveguide," *Opt. Exp.*, vol. 30, no. 7, pp. 10293–10305, 2022.
[18] Z. Wang, X. Xu, D. Fan, Y. Wang, H. Subbaraman, and R. T. Chen, "Geometrical tuning art for entirely subwavelength grating waveguide based integrated photonics circuits," *Sci. Rep.*, vol. 6, no. 1, 2016, Art. no. 24106.
[19] L. Sun, Y. Zhang, Y. He, H. Wang, and Y. Su, "Subwavelength structured silicon waveguides and photonic devices," *Nanophotonics*, vol. 9, no. 6, pp. 1321–1340, 2020.
[20] P. Cheben, R. Halir, J. H. Schmid, H. A. Atwater, and D. R. Smith, "Subwavelength integrated photonics," *Nature*, vol. 560, no. 7720, pp. 565–572, 2018.
[21] J. H. Song, T. D. Kongnyuy, P. De Heyn, S. Lardenois, R. Jansen, and X. Rottenberg, "Low-loss waveguide bends by advanced shape for photonic integrated circuits," *J. Lightw. Technol.*, vol. 38, no. 12, pp. 3273–3279, Jun. 2020.
[22] F. Gao et al., "Low-loss and compact bends on multi-layer SiN-on-SOI platform for photonic integrated circuits," *IEEE Photon. Technol. Lett.*, vol. 33, no. 20, pp. 1131–1134, Oct. 2021.
[23] L. Zhang et al., "Ultra-compact low-loss modified N-adjustable bends," *J. Lightw. Technol.*, vol. 41, no. 9, pp. 2792–2800, May 2023.
[24] L. Zhang et al., "Low-loss, ultracompact n-adjustable waveguide bends for photonic integrated circuits," *Opt. Exp.*, vol. 31, no. 2, pp. 2792–2806, 2023.
[25] P. Chamorro-Posada, "Silicon nitride bent asymmetric coupled waveguides with partial Euler bends," *Photonics*, vol. 11, no. 3, 2024, Art. no. 218.
[26] Y. Liu et al., "Very sharp adiabatic bends based on an inverse design," *Opt. Lett.*, vol. 43, no. 11, pp. 2482–2485, 2018.
[27] S. Sun, P. Dong, F. Zhang, J. Wang, N. Zhu, and Y. Shi, "Inverse design of ultra-compact multimode waveguide bends based on the free-form curves," *Laser Photon. Rev.*, vol. 15, no. 9, 2021, Art. no. 2100162.
[28] Z. Yu and X. Sun, "Inverse-designed photonic jumpers with ultracompact size and ultralow loss," *J. Lightw. Technol.*, vol. 38, no. 23, pp. 6623–6628, 2020.
[29] S. Irfan, J.-Y. Kim, and H. Kurt, "Ultra-compact and efficient photonic waveguide bends with different configurations designed by topology optimization," *Sci. Rep.*, vol. 14, no. 1, 2024, Art. no. 6453.
[30] W. Bogaerts and S. K. Selvaraja, "Compact single-mode silicon hybrid rib/strip waveguide with adiabatic bends," *IEEE Photon. J.*, vol. 3, no. 3, pp. 422–432, Jun. 2011.
[31] R. Shen et al., "Recent progress on inverse design for integrated photonic devices: Methodology and applications," *J. Nanophotonics*, vol. 18, no. 1, 2024, Art. no. 010901.
[32] J. L. P. Ruiz, F. Nabki, and M. Ménard, "Silicon nitride TM-pass polarizer using inverse design," *Opt. Exp.*, vol. 31, no. 23, pp. 37892–37899, 2023.
[33] J. L. P. Ruiz, A. A. Rabih, S. Nabavi, F. Nabki, and M. Ménard, "1 × 5 MEMS mode selective switch with an inverse-designed silicon nitride MDM," in *Proc. 2024 Opt. Fiber Commun. Conf. Exhib.*. 2024, pp. 1–3.
[34] J. Pita, F. Nabki, and M. Ménard, "Inverse-designed silicon nitride reflectors," *Opt. Lett.*, vol. 49, no. 4, pp. 786–789, 2024.
[35] M. Bahadori et al., "Design space exploration of microring resonators in silicon photonic interconnects: Impact of the ring curvature," *J. Lightw. Technol.*, vol. 36, no. 13, pp. 2767–2782, Jul. 2018.
[36] L. Su, R. Trivedi, N. V. Sapra, A. Y. Piggott, D. Vercruysse, and J. Vučković, "Fully-automated optimization of grating couplers," *Opt. Exp.*, vol. 26, no. 4, pp. 4023–4034, 2018.